

# Emission line oscillations in the dwarf nova V2051 Ophiuchi

D.Steeghs<sup>1,2</sup>, K.O’Brien<sup>2</sup>, Keith Horne<sup>2</sup>, Richard Gomer<sup>3</sup>, J.B.Oke<sup>4,5</sup>

<sup>1</sup> *Astronomy Group, University of Southampton, Highfield, Southampton, SO17 1BJ, UK (ds@astro.soton.ac.uk)*

<sup>2</sup> *Physics & Astronomy, University of St. Andrews, North Haugh, St. Andrews, KY16 9SS, UK (kso@st-and.ac.uk/kdh1@st-and.ac.uk)*

<sup>3</sup> *Howard Hughes Medical Institute and Department of Biochemistry and Cell Biology*

*Rice University, Houston TX 77005-1892, USA (richard@bioc.rice.edu)*

<sup>4</sup> *California Institute of Technology, Mail Stop 105-24, Pasadena, CA 91125, USA*

<sup>5</sup> *Dominion Astrophysical Observatory, Herzberg Institute of Astrophysics, National Research Council of Canada 5071 West Saanich Road, Victoria, BC V8X 4M6, Canada (bev.oke@hia.nrc.ca)*

Accepted 23 November 2000, Received 10 October 2000, in original form 26 May 2000

## ABSTRACT

We have detected coherent oscillations, at multiple frequencies, in the line and continuum emission of the eclipsing dwarf nova V2051 Ophiuchi using the 10m Keck II telescope. Our own novel data acquisition system allowed us to obtain very fast spectroscopy using a continuous readout of the CCD on the LRIS spectrograph. This is the first time that dwarf nova oscillations are detected and resolved in the emission lines. The accretion disc is highly asymmetric with a stronger contribution from the blue-shifted side of the disc during our observations. The disc extends from close to the white dwarf out to the outer regions of the primary Roche lobe.

Continuum oscillations at 56.12s and its first harmonic at 28.06 s are most likely to originate on the surface of a spinning white dwarf with the fundamental period corresponding to the spin period. Balmer and Helium emission lines oscillate with a period of 29.77s at a mean amplitude of 1.9%. The line kinematics as well as the eclipse constraints indicate an origin in the accretion disc at a radius of  $12 \pm 2R_{wd}$ . The amplitude of the emission line oscillation modulates (0-4%) at a period of 488s, corresponding to the Kepler period at  $R=12R_{wd}$ . This modulation is due to the beating between the white dwarf spin and the orbital motion in the disc.

The observed emission line oscillations cannot be explained by a truncated disc as in the intermediate polars. The observations suggest a non-axisymmetric bulge in the disc, orbiting at  $12R_{wd}$ , is required. The close correspondence between the location of the oscillations and the circularisation radius of the system suggests that stream overflow effects may be of relevance.

**Key words:** accretion, accretion discs – novae, cataclysmic variables – stars: individual: V2051 Oph – stars: oscillations

## 1 INTRODUCTION

Rapid variability is a tell-tale sign of accretion. The first coherent oscillation in a cataclysmic variable binary was reported by Walker as far back as 1956 (Walker 1956). The strictly periodic 71s brightness oscillations he found in DQ Her are now understood as being produced by a spinning magnetic white dwarf that is being fed by an accretion disc, and accretes the material along its magnetic field lines. Since the dynamical time scales of matter close to the white dwarf are of the order of tens of seconds, it was not until the development of high speed photon-counting photometers in the '70s that periodic signals were discovered in other systems.

The dwarf nova oscillations (DNOs) are periodic brightness modulations discovered in dwarf nova systems during outburst (Warner & Robinson 1972). The short time scales (2-40s) indicate an origin close to the white dwarf. In some systems, different periods were found at different times, and the period stability is considerably lower than the coherent oscillations in DQ Her. See Warner (1995) for review. Whereas the amplitudes in the optical are usually so low (< 1%) that the oscillations are only revealed after period analysis, Marsh & Horne (1998) detected coherent oscillations at two periods in the HST light curves of OY Car

with an amplitude of up to 20% towards the end of a super-outburst.

Reminiscent of the DNOs are the flood of QPOs reported in X-ray observations of accreting neutron star binaries (see van der Klis 2000 for review). The properties of these oscillations are in many ways very similar to those of DNOs, albeit on shorter time scales since these systems contain a much smaller compact object. It shows that moderately coherent oscillations appear to be a generic feature of accretion onto compact objects.

V2051 Ophiuchi is a short period eclipsing dwarf nova system belonging to the SU UMa sub-class. Its status as a dwarf nova was contested (e.g. Warner & O'Donoghue 1987) until two super-outbursts were observed in 1998 and 1999 by amateur variable star networks. Spectroscopy reveals double-peaked emission lines that exhibit a rotational disturbance effect during eclipse, corresponding to a prograde rotating accretion disc (Cook & Brunt 1983, Watts et al. 1986). Baptista et al. (1998) present a photometric model for the binary based on HST and ground based observations. Due to the unusual low-state the system was in during their observations, the orbital phases when bright spot and white dwarf are eclipsed by the mass donor star could be directly measured.

Warner & Cropper (1983) concluded that most of the rapid variability (flickering) was produced in the inner disc regions rather than the bright spot or white dwarf. The only quasi periodic oscillation in this system was reported by Warner & O'Donoghue (1987), who detected a very short lived 42s oscillation during outburst. It was not classified as a DNO because of its low coherence, and the absence of a corresponding spike in the power spectrum at that period. We present high time resolution spectroscopy of the dwarf nova V2051 Oph shortly after a normal outburst, obtained using our own data collection hardware equipped on Keck II, and report on the discovery of emission line oscillations at the level of several percent.

In the next Section we will describe the data acquisition system and novel reduction steps that were used. Section 3 covers the analysis of the data and discusses the properties of the oscillations. We discuss likely models in Section 4 and summarise our conclusions in Section 5.

## 2 OBSERVATIONS AND REDUCTION

The observations were obtained as part of a 5 night campaign to study rapid variability of cataclysmic variables and X-ray binaries (O'Brien 2000). The optical data were taken using the Low Resolution Imaging Spectrograph (LRIS; Oke et al. 1995) on the 10-m Keck II telescope on Mauna Kea, Hawaii between UT 7:22 and 7:57 on July 4th 1998. The LRIS was used with a 5.2 arc-second slit masked with aluminized mylar tape to form a square aperture. The 300/5000 grating used has a mean dispersion of 2.55 Å/pixel in the range 3600Å- 9200Å. We used a novel data acquisition system to obtain almost 28,000 2048 pixel spectra of V2051 Oph, in the form of a continuous data stream. Each spectrum has a mean integration time of 72.075 msec and there was no dead-time between individual spectra. Each 2048 pixel spectrum also contains a 25 pixel underscan region and a 75 pixel overscan region. The noise for a given pixel

was calculated using a readout noise of 6.3 e<sup>-</sup> and a gain of 4.7 e<sup>-</sup>/ADU. Cosmic rays were rejected with a threshold of 7-sigma from the de-biased frames. A master flat-field image was created by finding the median of 700 individual flat-field frames. This image showed no deviations above 0.3 % in all but 3 pixels. We decided that it was therefore not necessary to flat-field individual spectra. Calibration arc spectra were taken through the same slit aperture.

Background spectra, including light from the sky but dominated by a constant electronic background, were taken at the beginning and end of target observing, so that long time scale variations could be detected. The mean and variable components of the background spectrum were found by creating a light curve for each pixel and extracting the mean and gradient of this light curve. These coefficients were then filtered in wavelength, with a running median filter of width 101 pixels. The gradient of the data was found to be almost zero. The thus derived background spectrum, which accounts for ~ 0.9% of the total flux, was subtracted from each target spectrum.

The arc calibration was done by fitting a second order polynomial to 7 lines in a median spectra of exposures of Hg and Ar lamps. Arc spectra from the beginning and end of the exposures were used to take into account any drifts in the wavelength scale. The interpolated wavelength calibration was applied to each target spectrum using the MOLLY\* spectral analysis package. The spectrophotometric standard star, Feige 67 (Oke 1990) was observed using the identical setup. A low order polynomial fit was found to the median of all the individual flux star spectra and the individual target spectra were flux calibrated using MOLLY.

Individual time marks, accurate to 200ms, were placed after every other spectrum using the computer clock. In order to find the absolute times, secondary timestamps at known UT were placed at regular intervals throughout the observations. A calibrated UT radio clock was used for this purpose. With the help of these secondary timestamps, the times of each individual spectrum were calibrated, and we were thus able to achieve an absolute timing accuracy of close to 200ms.

To monitor seeing conditions and telescope tracking, the auto-guider CCD output was stored. We used this output to measure the position and FWHM of the guide star image every ~2s during our observations. Gaussian fits to the stellar images reveal very stable tracking and seeing conditions throughout our observations. A conservative estimate of the seeing was derived from the mean FWHM of the guide star images. This suggests that seeing was better than 0.8 arc-seconds, equivalent to a seeing limited FWHM resolution of our spectra of 3.7 CCD pixels.

## 3 DATA ANALYSIS

Occasionally, not all pixels of a spectrum were successfully transferred to the acquisition PC. These incomplete spectra were rejected from the data stream. In order to increase the

\* MOLLY is a 1D spectral analysis software package written and maintained by Dr.T.Marsh. Available for download at <http://www.astro.soton.ac.uk/~trm/software.html>

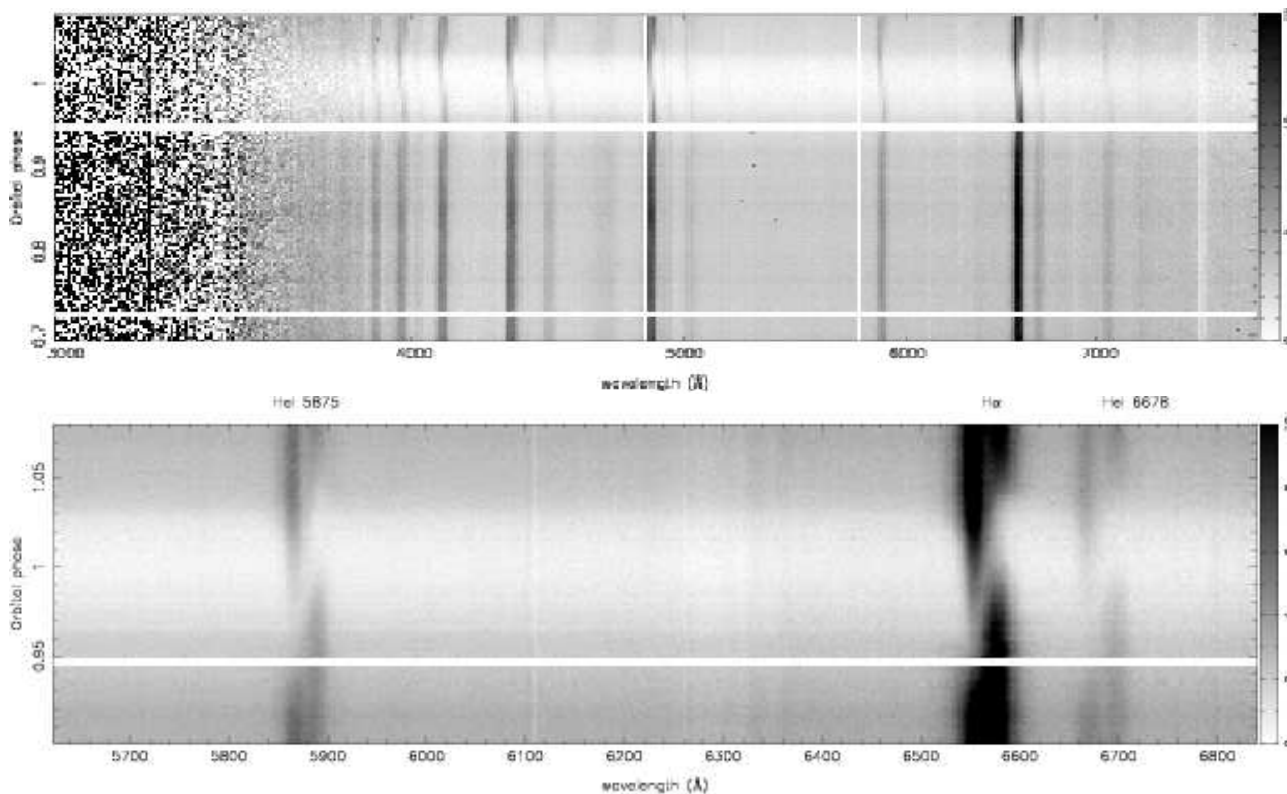


**Figure 1.** Top: trailed spectrogram of the whole data set after phase binning to 360 bins. The data are plotted on a logarithmic wavelength scale to provide a uniform velocity scale across the spectra. Gray scale denotes flux density in mJy. Bottom: A blow up of the eclipse of a few strong lines. Both Balmer and Helium lines show the classical pattern of the pro-gradely rotating accretion disc material being occulted by the companion star. Gaps occur at time of sky background measurements.

signal to noise of the remaining spectra and make the dataset more manageable, individual spectra were binned together in groups of 7 to give a final 3968 spectra with a time resolution of 0.5045 seconds. Since the dynamical timescale close to the white dwarf is of the order of a few seconds, this time resolution is still ample for our purposes. These spectra cover 40% of the binary orbit including an eclipse. The linear ephemeris of Baptista et al. (1998) was used to calculate orbital phases throughout this paper. Phase 0.0 corresponds to inferior conjunction of the companion star i.e. mid-eclipse.

Figure 1 shows a trailed spectrogram plot of the extracted spectra obtained covering the orbital phases between 0.69 and 1.08. The two gaps near phase 0.720 and 0.945 were introduced as the telescope was slewed to sky to allow robust sky subtraction as discussed above. Double-peaked emission lines are clearly visible, with the blue-shifted side of the lines eclipsing first, followed by the red-shifted peak, indicating the presence of a pro-grade rotating accretion disc.

A brightening of the object to  $V=13.2$  was reported by the VSNET<sup>†</sup> network on July the 2nd (VSNET Alert #1934). The usual quiescent brightness level of this dwarf nova is around  $V=15.7$ . This suggests a normal outburst was in progress in early July. Unfortunately, no measurements were available for the preceding week that could confirm

the exact start of the outburst. At the time of our observations, a  $V$  magnitude of 14.8 was reported, and 10 days after the observations the object was back to a quiescent level at  $V=15.7$ . It appears, therefore, we were observing V2051 Oph towards the later phase of decline from normal outburst.

### 3.1 The average spectral properties

Figure 2 (top) illustrates the average out of eclipse spectrum obtained by averaging all spectra between orbital phases 0.69 and 0.92. Strong broad disc emission lines are superposed on the flat continuum. The rapid drop in the spectral efficiency of the LRIS setup below  $4000\text{\AA}$  made it difficult to achieve robust flux calibration for bluer wavelengths. The Balmer jump appears to be in emission, however care must be taken with the flux scale in this region. The Balmer lines have a full width half maximum of  $2145 \pm 20\text{ km s}^{-1}$ , and the Balmer decrement from  $H\alpha$  to  $H\delta$  is 1:0.65:0.50:0.41, suggesting a mix of optically thick and thin emission. The Helium I lines are clearly double peaked and feature a slightly higher FWHM of  $2245 \pm 30\text{ km s}^{-1}$ . The blue peak is consistently stronger during this phase interval. Curiously, only  $H\alpha$  exhibits a slightly stronger red peak. This blue asymmetry is also present in the average spectrum of Watts et al. (1986) that covers  $H\beta$  and  $H\gamma$ , but not  $H\alpha$ . The  $H\alpha$  profile in Warner & O’Donoghue (1987) again shows a stronger red peak. This curious reversal of the double peak asymmetry seems to be a persistent feature of V2051 Oph. The line

<sup>†</sup> <http://www.kuastro.kyoto-u.ac.jp/vsnet/>

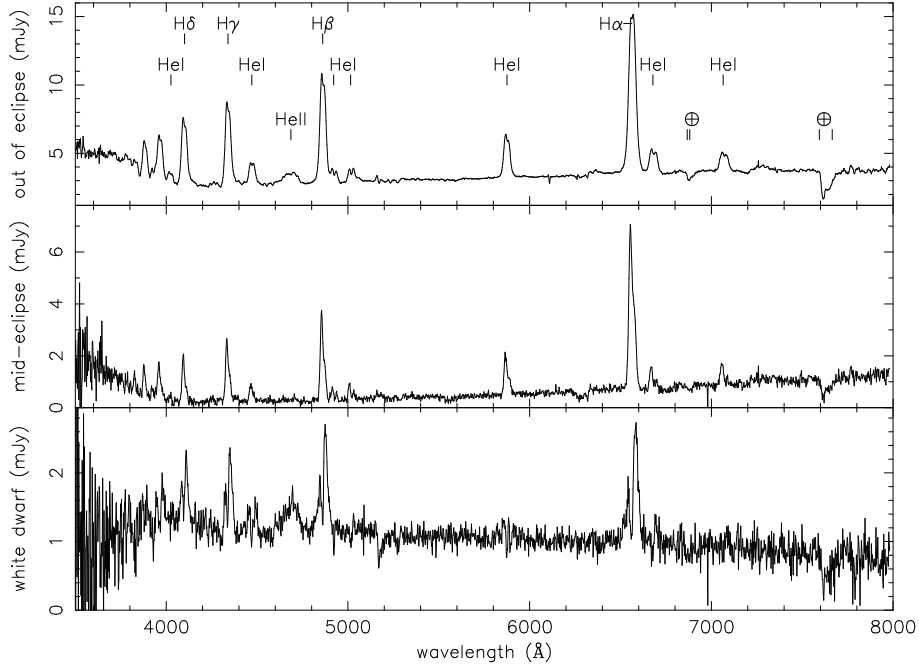


**Figure 2.** The average spectrum of V2051 Oph displays broad double-peaked Balmer and HeI emission lines. The top panel displays the out of eclipse spectrum obtained by averaging all spectra between orbital phases 0.69 and 0.92. The position of prominent lines as well as two telluric features red-wards of H $\alpha$  are marked. During mid-eclipse ( $0.995 < \phi < 1.005$ ), the continuum slope is slightly redder, and the emission lines only show the blue-shifted side of the disc as the red-shifted side is occulted from the observer (middle). The white dwarf contribution was isolated by subtracting the spectra on either side of white dwarf ingress and egress. It features a blue continuum and line emission from the accretion disc as the red-shifted part of the accretion disc is re-appearing (bottom).

wings extend out to at least  $3500 \pm 200 \text{ km s}^{-1}$  for both the Balmer and Helium lines.

Double Gaussians were fitted to the 6 strongest Balmer lines simultaneously. The double-peak separation was measured to be  $v_{sep} \sin i = 1120 \pm 60 \text{ km s}^{-1}$ , reflecting the radial velocities ( $\pm 560 \text{ km s}^{-1}$ ) of the gas on the outer edge of the accretion disc. If the velocity field of the disc is Keplerian and taking  $M_{wd} = 0.78 M_{\odot}$ ,  $R_{wd} = 0.0104 R_{\odot}$  for the mass and radius of the white dwarf (Baptista et al. 1998), then the orbital radius  $R_{kep}$  corresponding to this velocity  $v_{kep} = v_{sep}/2$  is given by :

$$R_{kep} = \frac{GM_{wd}}{v_{kep}^2} \sim 10^{10} \left( \frac{M_{wd}}{0.78 M_{\odot}} \right) \left( \frac{1000 \text{ km s}^{-1}}{v_{kep}} \right)^2 \text{ cm}$$

This gives an outer disc radius of  $R_{out} = 3.3 \times 10^{10} \text{ cm} = 45 \pm 4 R_{wd}$ . Although our estimated outer disc radius strictly exceeds the distance to L1 ( $R_{L1} = 42 R_{wd}$ ), tidal interactions will make the disc velocities sub-Keplerian and keep the disc within the primary Roche lobe. Similarly, the emission line wings indicate that disc emission extends to  $\sim 3500 \text{ km s}^{-1}$  corresponding to an inner disc radius of  $R_{in} \sim 8.4 \times 10^9 \text{ cm} = 1.2 \pm 0.2 R_{wd}$ . In order to confirm that the emission lines are indeed formed in the disc, we measured the eclipse behaviour of the emission lines as a function of velocity. We extracted light curves for each pixel between  $\pm 4250 \text{ km s}^{-1}$  of H $\beta$  and measured the eclipse half depth at ingress and egress (Figure 3). We see the blue-shifted side of the outer disc being eclipsed first followed by progressively smaller radii at larger velocities. The red-shifted disc emission is eclipsed later, with the outer edge disappearing just before mid-eclipse. The presence of a nearby HeI line at  $+3800 \text{ km s}^{-1}$  distorts

the measurements of the far red wing. Some uneclipsed light is present at low velocities. It is symmetric around zero velocity and has a FWHM of  $1000 \text{ km s}^{-1}$ . Also, the average time of mid-eclipse occurs significantly earlier than white dwarf conjunction. This has also been reported in IP Pegasi during outburst (Steeeghs 1999, Morales-Rueda et al. 2000). Analytical models for the velocity dependent eclipse phases of symmetric Keplerian discs are centered around phase 0.0 (e.g. Young, Schneider & Shetman 1981). These models are clearly not able to reproduce the observed eclipse behaviour of V2051 Oph, which suggests a strong disc asymmetry is present. The analysis demonstrates that most of the line emission is indeed produced in a pro-gradely rotating disc that extends from close to the white dwarf to the outer regions of the primary Roche lobe.

We isolated the mid-eclipse spectrum (Figure 2, middle) by averaging all spectra between orbital phases 0.995 and 1.005. As the relatively blue continuum from the inner disc is eclipsed, the cool companion star makes a larger fractional contribution, resulting in a slightly reddened continuum slope. Weak emission lines with a very strong blue shifted emission component are present, indicating that the eclipse is not total and some (outer) disc emission is still visible around these phases. The fact that the blue-shifted side is much stronger than the red-shifted peak, points to an asymmetry in the outer disc that was already visible as a persistent asymmetry in the out-of-eclipse line profiles. Either there is excess line flux produced in the blue-shifted side of the disc, or part of the red-shifted side is absorbed by a geometrically (and optically) thick structure.

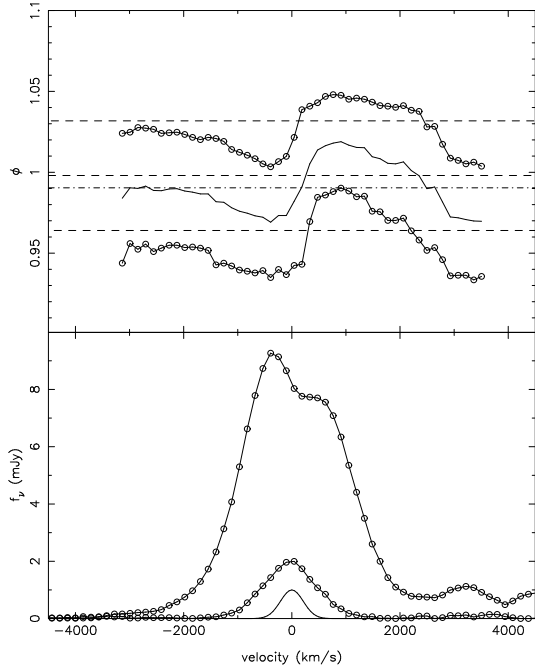


**Figure 3.** An analysis of the eclipse of the  $H\beta$  line emission. Half depth ingress and egress was measured for each pixel in the line profile. Top panel plots the measured values (dots) as well as the time for mid-eclipse for each velocity defined as the middle between ingress and egress (line). For comparison, the white dwarf contact phases and conjunction are indicated by dashed lines. The dot-dashed line indicates the average phase of mid-eclipse for the emission lines across the profile. Bottom panel is the out of eclipse flux of each velocity as well as the minimum flux density. The instrumental resolution is indicated as a Gaussian profile with height 1.

### 3.2 The white dwarf

In order to isolate the contribution from the white dwarf we subtracted the spectra from either side of white dwarf ingress and egress (Figure 2, bottom). To correct, to first order, for the changing contribution from the disc, we performed a linear fit to each wavelength pixel on a short section just before and after ingress. This fit was used to extrapolate the spectrum just before and after white dwarf ingress, and the white dwarf spectrum was obtained by taking the difference. The same procedure was applied at white dwarf egress, and the two derived white dwarf spectra, identical within the error bars, were averaged to derive our final white dwarf spectrum as plotted in Figure 2. Some emission line contribution from the disc is still present, although strong absorption cores of the Balmer lines are due to the white dwarf absorption line spectrum.

The blue slope reflects the continuum contribution expected from a hot white dwarf. Its relative contribution to the out-of-eclipse spectrum increases from  $\sim 15\%$  at  $8000\text{\AA}$  up to  $\sim 30\%$  at  $4000\text{\AA}$ . Black-body fits to the continuum shape indicates a white dwarf temperature around  $15000 \pm 2000$  K. Catalan et al. (1998) also derived a white dwarf temperature of  $15000\text{K}$  from HST FOS data.

In order to measure the contact phases of the white dwarf accurately, we applied the conventional method of using the derivative of the continuum light curve (e.g. Wood

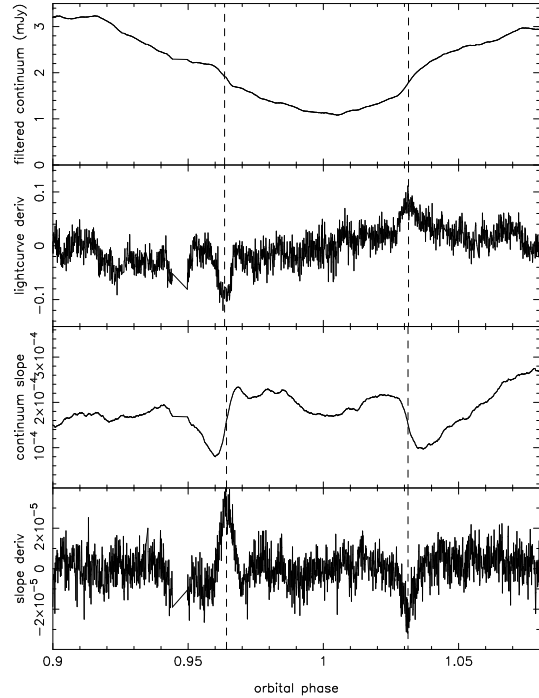


**Figure 4.** Measuring the white dwarf contact phases. Top panel is a filtered version of the continuum light curve followed by its derivative. The fitted ingress and egress phases are marked by vertical lines. For comparison we also fitted the continuum slope between  $4000$  and  $7000\text{\AA}$  as a function of orbital phase (positive slope indicates a red spectrum). The occultation of the white dwarf is marked by a sudden steepening as its blue spectrum is occulted (second panel from bottom). The derivative of this slope is again used to measure the ingress and egress phases (dashed lines, bottom panels).

et al. 1986). The light curve was first filtered with a running mean filter using a width of one third of the expected duration of the ingress and egress features. The numerical derivative was then calculated, and the ingress ( $\phi_{wi}$ ) and egress ( $\phi_{we}$ ) are defined as the orbital phases of minimum and maximum derivative (Figure 4). In order to determine these extrema, the derivative light curve was fitted with a Gaussian near the white dwarf features. The fitted centroids of these Gaussians are marked by vertical dashed lines.

To exploit the available spectral information, we also fitted the continuum slope of each spectrum with a first order polynomial. The ingress and egress features are expected to show up prominently on the continuum slope as the blue white dwarf spectrum is eclipsed/reappears. Figure 4 plots the derived continuum slope after filtering using the same filter that was used for the continuum light curve. The slope is a fit to all continuum sections between  $4000$  and  $6800\text{\AA}$ , with all the emission line regions masked out. A positive slope corresponds to a spectrum that increases towards red wavelengths. Indeed, white dwarf ingress and egress are easily identified as continuum slope changes. We performed a similar analysis to this light curve. The numerical derivative was calculated and the extrema were fitted with Gaussians.

From the ingress and egress phase we derived the duration of the white dwarf eclipse;  $\Delta\phi_{wd} = \phi_{we} - \phi_{wi}$  and the time of mid-eclipse  $\phi_0 = 1/2(\phi_{we} + \phi_{wi})$ . Our values (with a precision of  $\pm 2 \times 10^{-4}$ ) as well as the values deter-

**Table 1.** WD contact phases

	$\phi_{wi}$	$\phi_{we}$	$\Delta\phi_{wd}$	$\phi_0$
lightcurve	0.9635	1.0315	0.0680	0.9975
cont slope	0.9642	1.0313	0.0671	0.9978
mean	0.9639	1.0314	0.0676	0.9976
Baptista et al.	0.9670	1.0334	0.0662	1.00

mined by Baptista et al. (1998) are listed in Table 1. The two methods give compatible results, although the white dwarf ingress derived from the continuum slope is slightly later compared to the conventionally derived phase. We therefore averaged the results of the two methods to derive our final measurements. Our derived phases are systematically earlier compared to Baptista et al. (1998), indicating that the orbital ephemeris used is off by  $\sim 12$  seconds at the time of our observations. Our expected absolute time accuracy is better than 200ms, and this is therefore a significant difference. We did not attempt to construct a new orbital ephemeris but instead use our own measured white dwarf contact phases whenever needed as an internal calibration of the phasing. We also derive a larger value for  $\Delta\phi_{wd}$ , compared to Baptista et al. We remark that the system was observed just after outburst in our case, whereas Baptista et al. (1998) observed V2051 Oph during a rare low state.

### 3.3 Time variability

To study the rapid time variability of V2051 Oph we extracted orbital light curves from the phase resolved spectroscopy. All emission line regions were masked off to construct a continuum light curve spanning 4180–7960Å (Figure 5, top). We fitted a 3rd order spline to these continuum regions in order to determine the continuum shape and subtracted the fits from the data. From these continuum-subtracted spectra we then calculated emission line light curves. For the Balmer series we integrated all line flux within  $\pm 3500 \text{ km s}^{-1}$  from H $\alpha$ , H $\beta$ , H $\gamma$ , H $\delta$ , H $\epsilon$  and H8 using inverse variance weights to optimise the signal to noise in the resulting Balmer line flux light curve (Figure 5, middle). Similarly, we added the contributions of the six strongest Helium I lines marked in Figure 2 to construct a Helium light curve (Figure 5, bottom).

Apart from the deep eclipse that is visible in all light curves, there is also variability on short time scales. No prominent pre-eclipse hump is visible, although the limited phase coverage prevents a more robust analysis of the presence of bright spot emission in the light curves. The eclipses are not total, indicating some uneclipsed light is contributing to both the line and continuum emission (see also Figure 3). In particular, the emission line eclipses are highly asymmetric, and mid-eclipse occurs significantly before white dwarf conjunction. A strong disc asymmetry is apparently present, as expected earlier from the asymmetric emission line profiles. A blow up of a small section of each light curve reveals a clear periodic signal in the Balmer line light curve with a period around 30s. As expected, the continuum is also affected by non-periodic flickering, commonly observed in CVs. The measured white dwarf phases are marked as vertical dashed lines, and coincide with steep jumps in the continuum light curve.

In order to search for (quasi)periodic oscillations, Scargle power spectra were computed from the lightcurves. The slow orbital variations due to the eclipse were subtracted using a running mean filter with a length of 160 data points. The top panels in Figure 6 show the filtered light curve for the continuum and Balmer lines. Scargle power spectra between 0 Hz and the Nyquist frequency at 1 Hz reveal clear oscillations at low frequencies. In the continuum, aperiodic flickering results in a large amount of power below 0.02 Hz, i.e. on time scales of minutes - hours. The power rises steeply towards lower frequencies. A fit to the  $\log(\nu)$  versus  $\log(\text{Power})$  plot of the unfiltered continuum light curve revealed a power-law index of -2.1 for this flickering component, a common index observed in CVs (Bruch 1992). In Figure 6, this rising power at low frequencies is cut off by our filter. The peak at low frequencies in Figure 6 (top) is thus only a result of our filter and not an intrinsic peak in the power spectrum of the source. No significant power is present at the previously reported oscillation by Warner & O’Donoghue (1987) at 42.2s (0.024 Hz) in either the continuum or the Balmer lines. However two other frequencies stand out near 0.035 Hz. In the Balmer line power spectrum, these same two periods are the sole significant frequencies in the power spectrum. The position of the two frequencies ( $f_1=0.03359 \text{ Hz}$ ,  $f_2=0.03564 \text{ Hz}$ ) as well as their harmonics are marked by vertical lines in Figure 6. The continuum displays power at  $f_1$ ,  $f_2$  as well as  $f_2/2$  with similar power levels. Power at  $f_1/2$  is however absent. All of the peaks are well above the noise, as was confirmed by calculating an ensemble of power spectra while randomly jiggling the light curve points within their error bars. In order to check that the peak at  $f_2/2$  is not due to the increasing power at low frequencies, we used the fitted power law of the red noise (i.e. flickering) component mentioned above to measure the power in the peak relative to the red noise component (see also Figure 6). The power at  $f_2/2$  is at least a factor of  $\sim 3$  above the red noise component, so that its probability of occurring by chance is only  $\sim \exp[-3] \approx 0.05$ . Furthermore, cutting the light curve in several segments and calculating power spectra for each, shows the presence of both peaks near  $f_2$  and  $f_2/2$  in all segments. We are therefore confident that there are truly periodic components in the continuum light curve with the three frequencies  $f_1$ ,  $f_2$  and  $f_2/2$ .

The Balmer lines appear to oscillate solely at  $f_1$  and  $f_2$ . Interestingly, whereas  $f_2$  is stronger in the continuum,  $f_1$  is strongest in the Balmer lines. We could already identify a clear oscillation in the raw Balmer light curve with frequency  $f_1$  ( $1/f_1 = 29.8 \text{ s}$ , Figure 5). The amplitude of the oscillation varies considerably on a time scale of  $\sim 8$  minutes, almost disappearing completely at some phases. This amplitude variation reminds us of the beating behaviour between two closely spaced periods. With  $f_2 - f_1 = 0.00205 \text{ Hz}$  or a period of 8.1 minutes, it seems the two frequencies  $f_1$  and  $f_2$  are indeed connected by the beat frequency  $f_{beat} = f_2 - f_1$  corresponding to a beat period of  $P_{beat} = 488 \text{ s}$ .

The oscillations are coherent over our data segment. Since we cover only  $\sim 70$  emission line oscillations, we cannot put strong constraints to the coherency of the periods ( $> 10^2$ ) in order to compare them with the typical coherence levels of DNOs ( $10^4 - 10^6$ ).

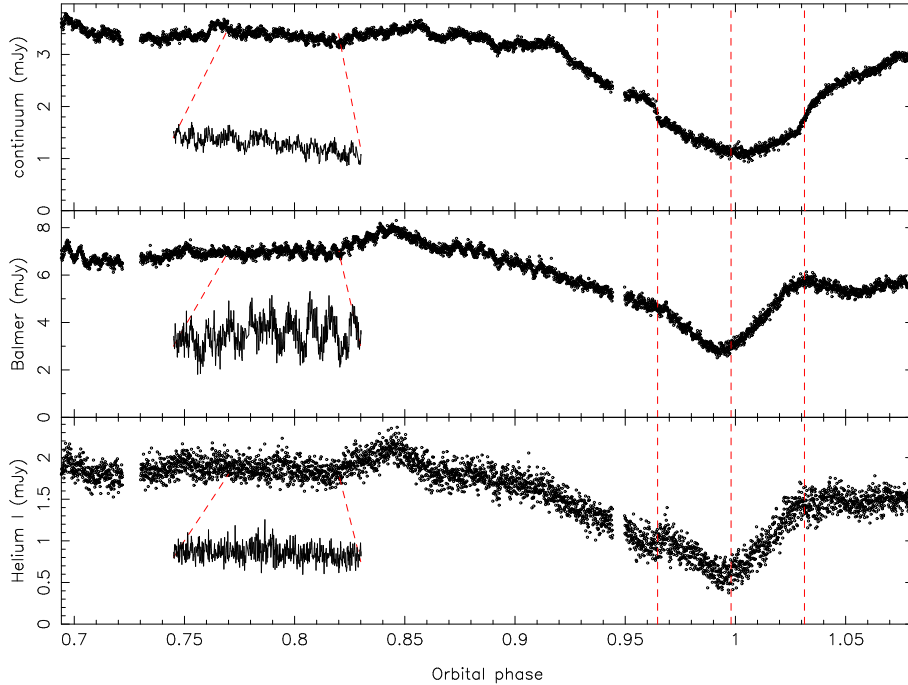


**Figure 5.** Orbital light curves of the continuum and line emission. From top to bottom, continuum, Balmer lines ( $H\alpha$ – $H8$ ) and He I line emission. For each light curve, a zoom of the section between phases 0.77 and 0.83 is also plotted. Vertical dashed lines denote white dwarf ingress, egress and conjunction.

### 3.4 The origin of the oscillations

The power spectra presented in the last section illustrated that there is a source driving the continuum and some line oscillations with a frequency of  $f_2$ . With equal power in the continuum at both  $f_2$  and its lower harmonic  $f_2/2$ , it appears that this driving source has  $f_2/2$  as fundamental frequency, corresponding to a period of  $P_2 = 2/f_2 = 56.12\text{s}$ . The emission lines mostly respond at the frequency  $f_1$  corresponding to a beat period of  $P_{beat} = 1/f_{beat} = 488\text{s}$  between  $f_2$  and  $f_1$ . Since all orbits in the binary are pro-grade, we expect only to see beats at lower frequencies ( $f_1 = f_2 - f_{beat}$ ) and not at  $f = f + f_{beat}$  if these periods are associated with orbital motions. This suggests that  $P_{beat}$  represents an orbital timescale associated with the emission line source.

In order to extract some spectral information concerning the oscillation sources, we folded all our spectra on the two periods  $P_1 = 2/f_1 = 59.53\text{s}$  and  $P_2 = 2/f_2 = 56.12\text{s}$ . The phase zero point was set to the time of the first data point in our data. Before phase folding the data, we subtracted a running mean from all spectra to remove the non-oscillating background spectrum. This was achieved by applying a running mean filter with a filter length of 120 spectra (60s) to the light curve at each wavelength pixel in the spectrum. Figure 7 plots the resulting trailed spectrograms for the two periods. On both periods, the continuum as well as the emission lines can be seen to oscillate.

In the emission lines, the oscillation source is crossing from blue to red twice within each 59s, forming a tiger stripe pattern in the folded trailed spectrogram. Curiously, the line emission is mostly visible going from blue shift ( $\sim -1000\text{ km s}^{-1}$ ) to red-shift ( $\sim 1000\text{ km s}^{-1}$ ). In  $H\alpha$ , the motions are strictly blue to red, the higher Balmer lines show a weak signature of a red to blue component as well.

In order to measure the velocity amplitude of the tiger stripe pattern, we combined the dynamical data of several lines. For comparison, Figure 8 plots the  $H\alpha$  emission on its own, the summed contribution of the higher Balmer lines  $H\beta$ – $H\epsilon$  as well as the sum of  $H\alpha$ – $H\epsilon$ . All Balmer lines share the same kinematics and phasing, though the  $H\alpha$  spectrogram may be slightly different from the higher Balmer lines. In order to measure the velocity amplitude ( $K$ ) of the spots, we measured the gradient ( $dv/d\phi$ ) of the tiger stripe as it is crossing zero velocity. If the spot traces a sinusoidal pattern as a function of phase, we then have  $K = \frac{1}{2\pi} \frac{dv}{d\phi}$  at zero. This resulted in an estimated velocity amplitude of  $K = 1210 \pm 80\text{ km s}^{-1}$  from  $H\alpha$ ,  $K = 1150 \pm 60\text{ km s}^{-1}$  from the higher Balmer lines and  $K = 1207 \pm 40\text{ km s}^{-1}$  from the sum of all the Balmer lines used.

The azimuthal velocity of the orbit with Kepler period 29.77s is  $2800\text{ km s}^{-1}$ , and clearly the emission line oscillations can therefore not be attributed to disc material orbiting at this Kepler period. However, we already associated the line source with the beat period of 488s. If this period is a Keplerian orbit, it corresponds to a velocity of  $1100 \pm 100\text{ km s}^{-1}$ , very close to the observed velocity amplitude of the emitting material.

### 3.5 Spectra of the oscillations

We extracted oscillation spectra from the phase-resolved spectroscopy  $F(\lambda, t)$ . This was achieved by fitting sine functions with frequency  $f$  of the form:

$$F(\lambda, t) = A(\lambda) \sin(2\pi ft + \phi(\lambda))$$

Here  $A(\lambda)$  represents the oscillation spectrum and  $\phi(\lambda)$  the phase angle which was allowed to vary for each pixel

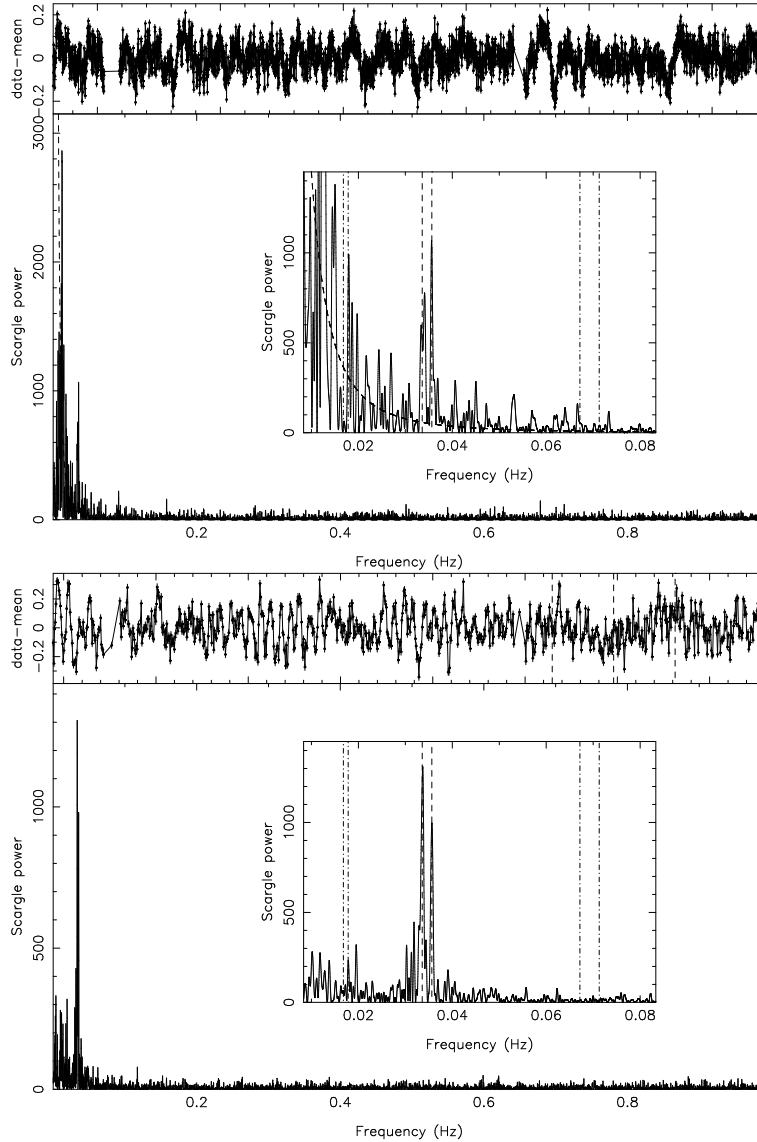


**Figure 6.** Power spectra calculated from the continuum (top) and Balmer light curves. The top panel in each plot is the light curve after filtering with a running mean. For plotting purposes, the data are binned by 4. Main panels are Scargle power spectra calculated from the un-binned filtered data. A zoom in of the region between 0.01 and 0.08 Hz illustrates the detected oscillations. Dashed lines denote the position of the two frequencies and their harmonics are marked by dot-dashed lines. For the continuum, a power-law fit to the red noise component is indicated by the dashed curve.

since. Figure 9 plots the fitted oscillation spectra obtained by fitting simultaneously to the frequencies  $f_1$  and  $f_2$ . We only used the data between phases 0.7 and 0.85 in order to avoid any problems with phase changes during eclipse. Since the signal to noise in the lines is much better compared to the continuum, we rebinned the spectra to obtain a minimum signal-to-noise of 50 in each bin. This allows us to keep narrow bins across the lines and wider ones for the continuum. Both continuum and lines oscillate at these periods as expected from the power spectra, with the lines achieving amplitudes of up to 5 times those of the continuum. Line emission modulated at  $f_1$  appears to come from slightly higher velocities compared to the emission from  $f_2$ , producing a clear double peaked emission line profile in the Balmer series and Helium lines. Since the phase angle is a free parameter for each pixel the amplitudes contain a pos-

itive bias. However, the continuum phases are constant as a function of wavelength, and continuum amplitudes can thus be reliably obtained from the orbital continuum light curves. In the next Section, we will look at the variation of the oscillation amplitudes as a function of orbital phase.

### 3.6 Eclipse constraints on the location of the oscillations

The eclipse provides valuable constraints on the possible locations of the oscillations. From the orbital light curves it is already clear that the line oscillations persist well into the eclipse. We constructed two Balmer emission line light curves to separate the blue-shifted and red-shifted emission. From the continuum-subtracted spectra we integrated all line flux between  $-3500$  and  $0 \text{ km s}^{-1}$  of  $H\alpha - H8$ . Similarly,



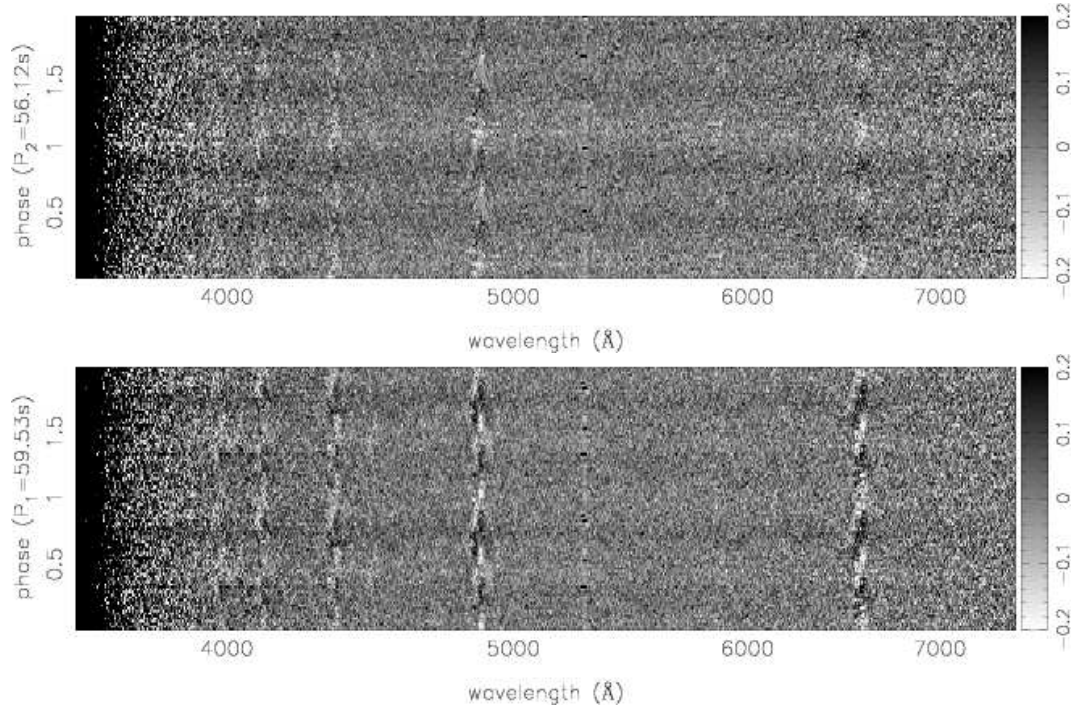


**Figure 7.** The data folded on the two oscillation periods after applying a running mean filter to subtract the non-oscillating background spectrum. Top panel plots two cycles of the period  $P_2 = 56.12\text{s}$ , with two cycles of the slightly longer period  $P_1 = 59.53\text{s}$  at the bottom. A log wavelength scale is plotted to provide a constant velocity scale.

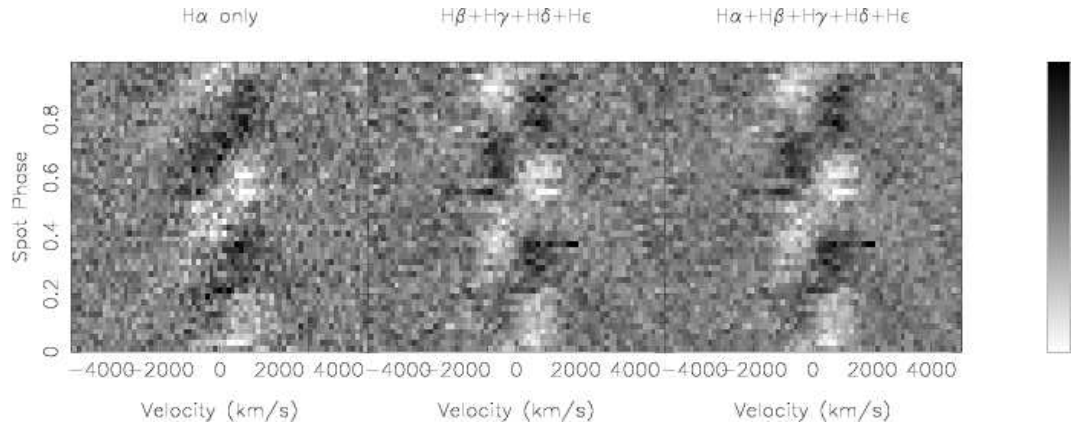


**Figure 8.** The data folded on the oscillation period  $P_1 = 59.53\text{s}$ . We combined several Balmer lines to boost the signal. Top left the  $\text{H}\alpha$  trailed spectrogram, middle is the sum of  $\text{H}\beta$ ,  $\text{H}\gamma$ ,  $\text{H}\delta$  and  $\text{H}\epsilon$ , and right panel is the sum of  $\text{H}\alpha$ - $\text{H}\epsilon$ . All Balmer lines indicate identical line kinematics across the spot phase.

we constructed a light curve for all the red-shifted line emission between 0 and  $+3500\text{ km s}^{-1}$ . These light curves were then filtered again by a running mean filter of 80 points. We then fitted sinusoids to sections of the light curves to determine the amplitudes and phase of the oscillation as a function of orbital phase. Since the two frequencies are so close to each other, it was not possible to reliably fit the amplitudes of two frequencies simultaneously. Instead we fitted the amplitude of the strongest line oscillation at  $P_1/2$  (29.8s). Figure 10 shows the derived amplitudes for the blue and red light curves as well as a re-binned version of the two light curves to illustrate the modulations in amplitude directly. The amplitudes peak at a level of  $\sim 4\%$  and mod-

ulate regularly with the beat period of  $\sim 8$  minutes. There also appears to be a general trend of a gradual drop in the oscillation amplitudes across the data, indicating the oscillation has a limited lifetime. The oscillation in the blue wings drops down around orbital phase 0.93, and only slowly recovers after mid-eclipse. On the other hand the oscillations persist in the red wing until mid-eclipse, well past the white dwarf ingress at phase 0.963. This indicates that the site of the emission line oscillations cannot be confined to the white dwarf, but needs to be located at a considerable distance from it. Only red-shifted emission from the oscillation is visible during the early parts of the eclipse. This is in accordance with an origin as a pro-grade rotation in the disc,

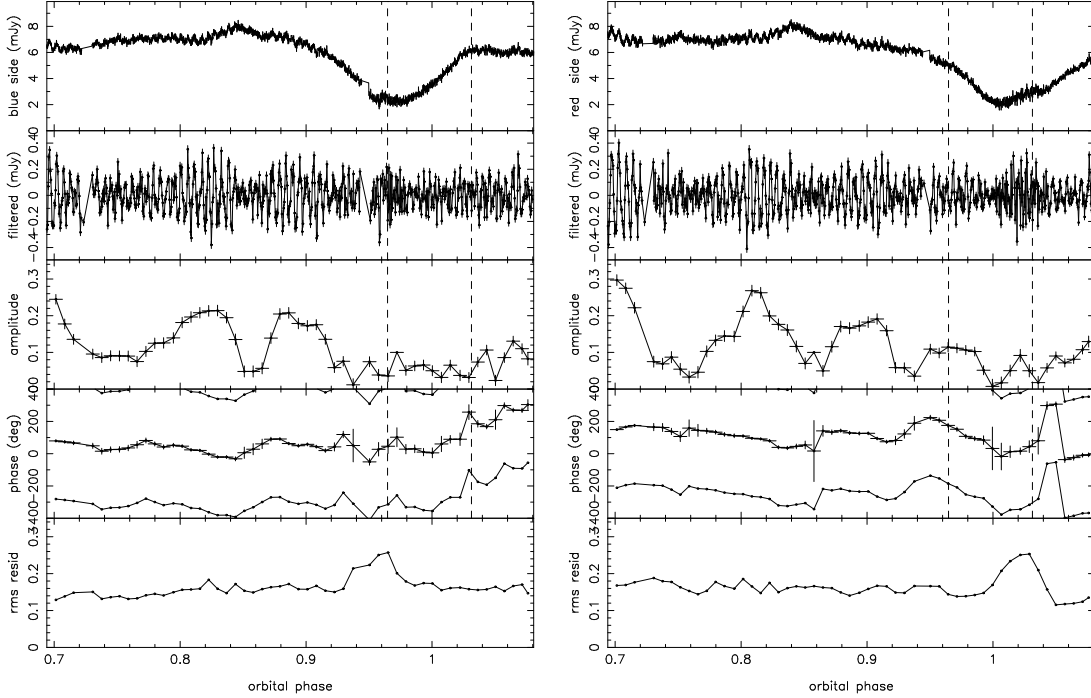


**Figure 10.** The Balmer oscillation amplitudes separated into blue-shifted (left) and red-shifted emission. Top panels show the unfiltered light curves, followed by a filtered and binned version to highlight the oscillations. The amplitude variation can be directly identified in the two light curves. Sliding sine fits to the data were used to obtain a light curve of the oscillation amplitude. The fitted amplitudes and phases constitute the next two panels. Final panel plots the RMS of the fit residuals after the sine-fit is subtracted from the data. Dashed lines mark white dwarf ingress and egress.

since the blue-shifted part is already eclipsed, but the red-shifted part is still visible. This also fits in well with the observed kinematics of the emission lines (Section 3.4, Figures 7, 8 and 9). The corresponding Kepler orbit is at a distance of  $12 \pm 2R_{wd}$ . The phases of the oscillation modulate in sync with the amplitude changes across each beat cycle with a variation of  $\sim 100^\circ$ . The blue side consistently advances the red by  $\sim 90^\circ$ . If the emission line is indeed produced by material in the disc, phase changes are expected as the emitting material orbits around the white dwarf. During eclipse both sides show a large change in the phasing of the oscillation as part of the oscillating source is eclipsed, with the two sides being out of phase by roughly  $\sim 280^\circ$  at the end of our data. We also calculated the RMS of the fit residuals after the sine fit was subtracted from the data. The RMS light curve shows a short interval of increased variability, near white dwarf ingress for the blue side, and near egress for the red-shifted side. It appears to originate from the small area of the inner disc that is still visible, in between the Roche lobe of the companion and the white dwarf. The variability is not periodic and we do not seem to see similar variability from the side of the disc on the other side from the white dwarf (i.e. at egress for blue and ingress for red).

The amplitude/phase measurements for the continuum oscillation were more complicated to extract. First of all, as can be seen from the oscillation spectra, the amplitude of the continuum oscillation is typically about a factor 5 weaker, and there is also a lot of aperiodic variability in the continuum superposed on the oscillation. Since the phasing of the oscillation appears to be wavelength independent (Figure 9), we do not need to split the continuum emission up

**Table 2.** Fitted oscillation amplitudes

	amplitude range	mean amp
Balmer lines	0.01-0.26 mJy (0.0-3.7%)	0.11 mJy (1.9%)
continuum	0.00-0.04 mJy (0.0-2.%)	0.022 mJy (0.8%)

into wavelength bands, and can use the orbital continuum light curve we derived before. The continuum light curve was first filtered using a running mean to remove the slower aperiodic variations to first order. Sine functions were then fitted at the continuum oscillation period of  $P_2 = 56.12s$ . Unfortunately, the continuum was clearly affected by other aperiodic variability as the fits were poor with high  $\chi^2$  values ( $\sim 3-5$ ) and large RMS residuals. The oscillation amplitude and phase varies considerably both during eclipse as well as out of eclipse. During eclipse the amplitudes drop and are compatible with zero. However, no sharp eclipse of the oscillation was apparent that could firmly establish an origin on the white dwarf itself. The amplitude light curve of the continuum oscillation is therefore not accurate enough to distinguish between a location on the white dwarf itself or close to it in the disc.

Table 2 lists the oscillation amplitude ranges obtained from these sine fits to the Balmer lines and the continuum. Although the continuum oscillation is much weaker compared to the lines, both reach maximum relative amplitudes of a few percent. We have obtained some strong constraints to the origin and location of the continuum and emission line oscillations. In the next section we review several possi-

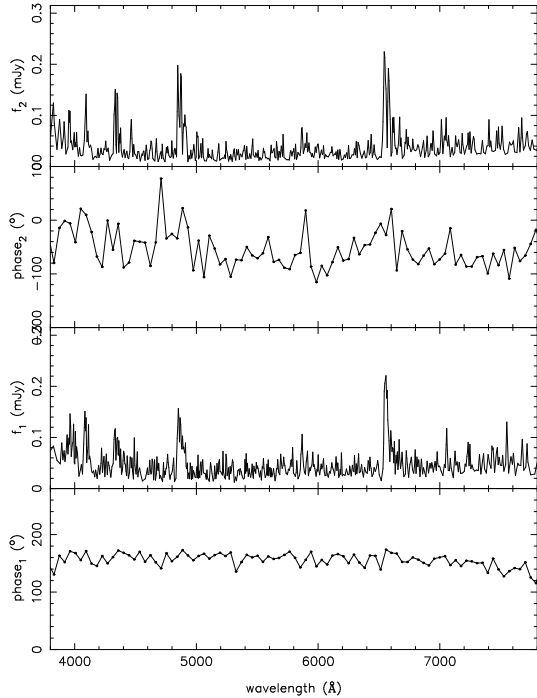


**Figure 9.** The spectrum of the oscillation obtained by fitting sine-functions to the data for each pixel. Top two panels are spectrum of the oscillation with frequency  $f_1$  and the phase angle, the bottom two panels correspond to  $f_2$ . The oscillation spectra are rebinned to achieve a minimum signal to noise in each spectral bin of 50 in order to exploit the better s/n in the lines compared to the continuum.

ble models for the observed oscillations, and see if they are able to satisfy the above constraints.

## 4 INTERPRETATION

Before reviewing possible explanations for the observed oscillations, let us quickly summarise the main features that a model must satisfy in order to explain the observations. In the continuum we observe oscillations at 56.12s and its harmonic at 28.06s, that must originate close to the white dwarf or on the compact object itself. The emission lines oscillate mostly at 29.77s, and require a source at a distance of  $\sim 12R_{wd}$ , corresponding to an orbital period of 488s, which is also the beat period between 29.77s and 28.06s. The emission line oscillation amplitudes modulates regularly on the beat period of 488s and emission is only visible going from maximum blue-shift to red-shift, but not vice-versa.

### 4.1 Pure disc oscillations?

Over the years various models have been proposed that attribute the DNOs to oscillations or modes in the disc itself. Possible mechanisms are non-radial pulsations (e.g. van Horn, Wesemael & Winget 1980), axisymmetric radial pulsations (Kato 1978), vertical oscillations or resonant oscillations due to shock waves (Molteni et al. 1996). In most cases, the oscillation period is to first order the local Keplerian period. We can then obviously connect each observed frequency to a particular radius in the disc which gives orbits

between 1 and 3 white dwarf radii out for the observed oscillations. For example,  $P_2$  corresponds to a Kepler orbit at  $R = 2.8R_{wd}$ , and its harmonic is at  $R = 1.8R_{wd}$ . However, there is no particular reason why the disc would oscillate at these distinct radii, and not at some other, and no explanation of how it manages to do so coherently. Also, the presence of the harmonic of  $f_2$  but not  $f_1$  is not explained, nor is the connection between  $f_1$ ,  $f_2$  and the observed beating behaviour with a period of 488s. More seriously, we showed in Section 3 that the emission line oscillation originates at  $12R_{wd}$ , but oscillates with a period of 29.77s, which is not the local Kepler period. Although we have established that the emission line oscillation requires an origin in the disc, which is an important result in itself, a model relying on disc modes only seems unsatisfactory.

### 4.2 White dwarf pulsations

The emission line oscillation cannot originate from the white dwarf itself, but the continuum oscillations at  $P_2$  and  $P_2/2$  are indeed expected to be related to the white dwarf. One possible mechanism that can produce periodicities apart from a fixed structure on a rotating white dwarf, is oscillations of the white dwarf.

Papaloizou & Pringle (1977) discussed non-radial oscillations of rotating stars and concluded that oscillations in rotating white dwarfs can indeed produce the oscillations at periods corresponding to DNOs. The periods of these modes with order  $m$  is  $\sim P_{spin}/m$ , with  $P_{spin}$  the spin period of the white dwarf, and in principle any number of orders can be superposed at any given time. It is thus not obvious how one mode will stand out compared to the others and produce a single, coherent spike in the power spectrum.

The detected power at  $P_2$  and  $P_2/2$  could thus, in principle, be interpreted as the incarnation of two orders of a non-radial oscillation on the white dwarf. However, two equatorial spots on a rotating white dwarf with spin period  $P_2$  could explain the observations just as well. The latter would also explain the observed beating behaviour between the spinning white dwarf and orbiting disc material more naturally. One way to distinguish between these two models would be the detection of other periods, but not  $P_2$ , in this system. In the case of white dwarf oscillations it is easy to produce power at different orders and modes, however the white dwarf spin period cannot be changed on short time scales and should leave a persistent signature.

Another class of models that relies on the origin of the DNOs close to the white dwarf are differentially rotating surface layers above the white dwarf (Warner 1995), or interaction between the disc and the boundary layer around the white dwarf (e.g. Popham 1999). The main concern with these models, when trying to understand the behaviour of V2051 Oph, is that they can in principle account for the oscillations that originate close to the white dwarf ( $f_2$ ,  $f_2/2$ ), but not the emission lines oscillation ( $f_1$ ).

### 4.3 An intermediate polar scenario

Emission line oscillations have been seen so far only in the CV sub-class of intermediate polars such as DQ Her (Martell et al. 1995) and RXJ0558 (Harlaftis et al. 1999). In these

systems, the magnetic white dwarf accretes via two hot spots at its magnetic poles as it spins rapidly. The disc is truncated at the radius where magnetic pressure is comparable to the gas ram pressure, and the gas flow makes a transition from Keplerian motion in the plane to a motion along field lines. The observed line oscillations are produced by disc material that is illuminated by the hot spots on the white dwarf as they sweep by.

However, if we try to interpret the observed oscillations in V2051 Oph in terms of this model, it fails for several reasons. We have established that the emission lines are formed in the disc which extends from very close to the white dwarf out to the outer edges of the primary Roche lobe. The emission line oscillation is produced in the disc at  $\sim 12R_{wd}$ , but the disc is clearly not truncated there. In this model,  $P_2$  is the spin period of the white dwarf, which leads to a co-rotation radius of  $R_{co} = 2.8R_{wd}$ . Apart from the fact that the disc apparently extends down to the white dwarf, the system would be a propeller and any material threading at  $R \sim 12R_{wd}$  would be propelled out. Finally, in the intermediate polars we observe the emission lines as they move from red-shift to blue shift and not vice versa as in the case of V2051 Oph. If we would interpret the observed line oscillation kinematics (Figures 7,8) in terms of material moving along magnetic field lines rather than in the disc, we wouldn't see the blue wing oscillations being eclipsed first followed by the red wing at mid-eclipse (Figure 10). The intermediate polar scenario therefore fails in the sense that the emission line oscillations cannot originate from the edge of a truncated disc as in DQ Her and RXJ0558 or from a magnetic curtain. However, the system may well contain a weakly magnetised white dwarf with two active magnetic poles that is responsible for the oscillations at  $f_2$  and  $f_2/2$ . However, this cannot account for the emission line oscillations at 29.77s.

#### 4.4 A spinning white dwarf illuminating the disc

We have reviewed some possible models that could explain the observed set of oscillations in V2051 Oph. The continuum oscillations at  $f_2$  and  $f_2/2$  are most naturally explained by a spinning white dwarf with  $P_{spin} = P_2$  containing two hot spots, that produce a modulation at the spin period and its harmonic. The origin of these hot-spots may be due to a weak magnetic field of the primary, which is low enough such that the disc can still extend to close to the white dwarf. The radiation from these two spots illuminates the disc, and is reprocessed as continuum and line emission at a radius of  $\sim 12 \pm 2R_{wd}$ . The corresponding emission oscillates at the beat frequency between the spin of the white dwarf and the local Kepler period of 488s producing line oscillations at 29.8s.

We noted before that we only see line emission going from blue shift to red shift and not vice-versa. This may be caused by the presence of material close to the white dwarf above the disc plane, that absorbs the line emission when it is on the far side of the disc from the point of view of the observer, but not when it is in front. One candidate for this is the uneclipsed light. Alternatively, the emission of orbiting material could be beamed an-isotropically, only producing line emission away from the white dwarf. Orbiting material would then only be visible going along the front

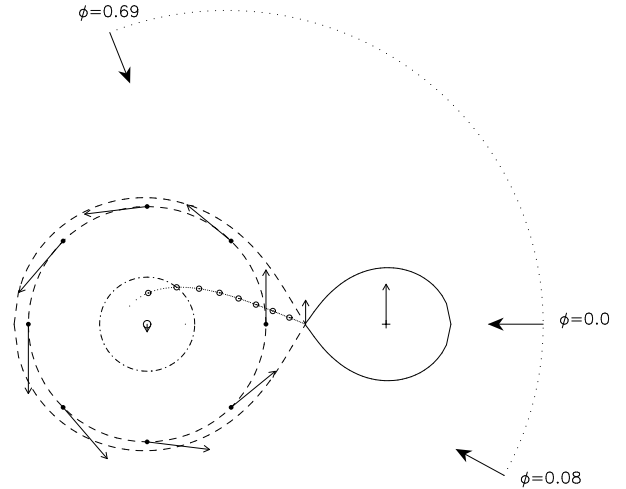


**Figure 11.** A top view of V2051 Oph with the mass donor star on the right. The ballistic stream trajectory is plotted down to its point of closest approach to the white dwarf. The dot-dashed line is the site of the emission line oscillations and corresponds to the circularisation radius. The arrows on the outer disc denote the local direction of the Kepler flow. The arc on the outside illustrates the orbital phases during which the system was observed (time increasing clockwise).

side. Perhaps the inner side is blasted by the white dwarf and is too hot to produce optical line emission, whereas the outer side is at low enough temperatures to emit Balmer and Helium emission.

What remains to be explained is why does this processing occur at this specific radius, and why does it modulate its amplitude regularly? Since the orbiting disc material at this radius is beating with the white dwarf spin, it needs to be a localised region, both in terms of radius as well as azimuth, that is mostly responding for it to produce a coherent oscillation. A localised 'bulge' in the disc at the required radius would orbit the disc every 488s and its oscillation amplitude would modulate because of the intervening gas that prevents us from viewing the bulge when its on the far side. This obscuring material that was required to explain the blue-to-red pattern in the emission lines, thus also explains the regular modulation of the amplitude every 488s. Popham (1999) also invoked a non-axisymmetric bulge in the disc to produce DNOs. In his model, the bulge is formed at the transition radius between the disc and the boundary layer surrounding the white dwarf. In our case, the bulge is clearly too far from the white dwarf to be due to such a boundary layer-disc interaction. We are now in the familiar, and unfortunate, position again that one needs to invoke some unknown mechanism in order to produce a structure in the disc at this specific radius.

Figure 11 plots a schematic top view of the binary, with the site of the line oscillation marked as a circle. We calculated a few characteristic radii for V2051 Oph, using the binary parameters of Baptista et al. (1998). For example, we couldn't connect this radius with a tidal resonance. However, the circularisation radius for this system is (Warner 1995);

$$R_{circ} = 0.0859q^{-0.426}a = 7.8 \times 10^9 \text{ cm} \sim 11 \pm 2R_{wd}$$

This close correspondence between the emission line source

and the circularisation radius suggests that gas stream effects may be of relevance. Lubow (1989) explored the possibility of stream overflow, and in the case of no disc interaction streamlines typically re-impact in the orbital plane at the radius of closest approach;

$$R_{min} = 0.0488q^{-0.464} a = 4.9 \times 10^9 \text{ cm} \sim 7 \pm 1R_{wd}$$

The exact nature of the stream-disc interaction is not well understood, but we may expect some stream-disc effects between these two radii. The attractive feature of such a stream overflow would be the natural way in which a vertically extended structure would be present at roughly the right radius to produce the reprocessed emission. We also noted in section 3.1 that near mid-eclipse the blue shifted contribution from the disc is persistently stronger compared to the red-shifted emission. Stream overflow would block part of the red-shifted disc emission from view, and this asymmetry could thus be easily accommodated. The reversal of this asymmetry in the H $\alpha$  remains a puzzle, however.

It is clearly not trivial to produce a localised bulge in the disc at this stream impact location, that is able to orbit coherently for quite some time while stream overflow is occurring. Observations of this kind spanning longer intervals, could shed some light on the coherency of such structures. A more thorough simulation of such a scenario is also required in order to test if such a geometry is a viable way of producing the observed oscillations (and perhaps other DNOs). This is beyond the scope of this paper, but such a scenario does appear to be able to accommodate all the features of the observed oscillations. Since we observe the system towards the end of an outburst, the radial density distribution is not expected to be that of a steady-state disc. Disc instability calculations usually show a broad peak in the density at roughly the circularisation radius towards the end of the outburst. Such an 'empty' disc would be in particular susceptible to stream overflow, and again the obvious region for stream-disc interaction would be near the circularisation radius where the density peaks and the stream is flowing towards the orbital plane again.

## 5 CONCLUSIONS

We detected coherent continuum and emission line oscillations in the dwarf nova V2051 Oph on decline from a normal outburst. Accretion disc emission extends from very close to the white dwarf out to the outer parts of the primary Roche lobe. The disc emission lines display a persistent blue to red asymmetry, with the blue peak being stronger in all the Helium lines as well as the Balmer lines, except H $\alpha$  which has a stronger red peak. The eclipse light curves are also highly asymmetric which suggests that the blue side of the disc makes a larger contribution to the emission compared to the red-shifted side.

The continuum oscillations are most likely to originate on the surface of a spinning white dwarf with spin period 56.12s and temperature around 15000K. The amplitude of the oscillation in the continuum varies between 0 and 4%, and disappears during white dwarf eclipse. The Balmer and Helium I emission lines oscillate strongly at a period of 29.8s. The line kinematics as well as the eclipse constraints indicate these to come from a non-axisymmetric bulge in the disc at

a radius of  $12 \pm 2R_{wd}$ . The corresponding Kepler orbit has a period of 488s, and corresponds well with the observed amplitude variations (0-4%) on this period. The oscillating line emission is observed to go from maximum blue-shift to maximum red-shift every 29.8s, but not vice versa. This, together with the regular modulation of the oscillation amplitudes can be explained by intervening gas above the orbital plane, close to the white dwarf. This is supported by an un-eclipsed component in both the continuum and lines. In the Balmer lines this component is centered on zero velocity and has a FWHM of 1000 km s<sup>-1</sup>. Alternatively, the emission is beamed away from the white dwarf.

The close correspondence between the location of the oscillations and the circularisation radius of the system as well as the disc asymmetry may indicate the relevance of stream overflow to the presence of vertically extended bulges in the disc. More observations of this kind as well as more detailed simulations of such a scenario are required to confirm its feasibility in the light of producing DNOs. Predictions of our interpretation are the persistent presence of 56.12s/28.06s oscillations from the white dwarf. This period should be detected at other epochs, most likely in the UV. The UV also provides opportunities to measure the spin of the white dwarf directly using the rotational broadening of white dwarf absorption lines (Sion 1999). With a spin period of 56.12s, the expected surface velocity of the spinning white dwarf works out to be:

$$v_{wd} = \Omega \times R_{wd} = 2\pi/P_2 \times R_{wd} = 810 \text{ km s}^{-1}$$

Secondly, we expect the period of the emission line oscillations to change across the outburst cycle as the location and extent of stream overflow and re-impact will depend on the radial density distribution of the disc. For example, if we wish to interpret the reported 42.2s oscillation (Warner & O'Donoghue 1987) in this scenario, it can be identified as the beat between the white dwarf spin and a Keplerian orbit at  $\sim 7R_{wd}$ .

The data presented here demonstrate the potential of high speed spectroscopy of CVs using large aperture telescopes. We detected emission line oscillations in a dwarf nova for the first time, and located their origin in the accretion disc. A better understanding of the elusive DNOs would benefit from a high time resolution study of (eclipsing) dwarf novae across their outburst cycle.

## ACKNOWLEDGEMENTS

Data presented herein were obtained at the W.M. Keck Observatory, which is operated as a scientific partnership among the California Institute of Technology, the University of California and the National Aeronautics and Space Administration. The Observatory was made possible by the generous financial support of the W.M. Keck Foundation. We thank Tom Marsh for the use of his MOLLY analysis software, and for many useful discussions. Lars Bildsten, Graham Wynn, Phil Charles, Jenő Sokolovski and Rob Hynes are thanked for their comments and suggestions. We thank the referee for his/her useful comments and suggestions. DS was supported by a PPARC Fellowship during part of this research.

## REFERENCES

- Baptista, R., Catalan, M. S., Horne, K., Zilli, D., 1998, MNRAS, 300, 233
- Bruch, A., 1992, A&A, 266, 237
- Catalan, M.S., Horne, K., Cheng, F.H., Marsh, T.R., Hubeny, I., 1998, ASP Conf. Series 137, *Wild stars in the Old West*, p426
- Cook, M.C., Brunt, C.C., 1983, MNRAS, 205, 465
- Harlaftis, E.T., Horne, K., 1999, MNRAS, 305, 437
- Kato, S., 1978, MNRAS, 185, 629
- Lubow, S.H., 1989, ApJ, 340, 1064
- Marsh, T.R., Horne, K., 1998, MNRAS, 299, 921
- Martell, P.J., Horne, K., Price, C.M., Gomer, R., 1995, ApJ, 448, 380
- Molteni, D., Sponholz, H., Chakrabarti, S.K., 1996, ApJ, 457, 805
- Morales-Rueda, L., Marsh, T.R., Billington, I., 2000, MNRAS, 313, 454
- O'Brien, K., 2000, Ph.D thesis, University of St.Andrews
- Oke, B., 1990, AJ, 99, 162
- Oke, B., Oke, Cohen, J. G., Carr, M., Cromer, J., Dingizian, A., Harris, F. H., Labrecque, S., Lucinio, R., Schaal, W., Epps, H., Miller, J., 1995, PASP, 107, 375
- Popham, R., 1999, MNRAS, 308, 979
- Sion, E., 1999, PASP, 111, 532
- Steeghs, D., 1999, Ph.D thesis, University of St.Andrews
- van der Klis, M., 2000, ARAA, 38
- van Horn, H.M., Wesemael, F., Winget, D.E., 1980, ApJ, 235, 143
- Young, P.J., Schneider, D.P., Sheckman, S.A., 1981, ApJ, 244, 259
- Walker, 1956, ApJ, 123, 68
- Warner, B., Robinson, E., 1972, Nat.Phys.Sci., 239, 2
- Warner, B., Cropper, M., 1983, MNRAS, 203, 909
- Warner, B., O'Donoghue, D., 1987, MNRAS, 224, 733
- Warner, B., 1995, *Cataclysmic Variable Stars*, Cambridge Astrophysics Series 28, Cambridge University Press
- Watts, D.J., et al., 1986, A&A, 154, 197
- Wood, J.H., Horne, K., Berriman, G., Wade, R., O'Donoghue, D., Warner, B., 1986, MNRAS, 219, 629